Emergence of the Chern Supermetal and Pair-Density Wave through Higher-Order Van Hove Singularities in the Haldane-Hubbard Model

Pedro Castro, Daniel Shaffer, Yi-Ming Wu, and Luiz H. Santos

Phys. Rev. Lett. **131**, 026601 — Published 11 July 2023

DOI: 10.1103/PhysRevLett.131.026601

Emergence of Chern Supermetal and Pair-Density Wave through Higher-Order Van Hove Singularities in the Haldane-Hubbard Model

Pedro Castro,[1] Daniel Shaffer,[1] Yi-Ming Wu,[2] and Luiz H. Santos[1]

[1]*Department of Physics, Emory University, 400 Dowman Drive, Atlanta, GA 30322, USA*
[2]*Stanford Institute for Theoretical Physics, Stanford University, Stanford, California 94305, USA*

(Dated: May 24, 2023)

While advances in electronic band theory have brought to light new topological systems, understanding the interplay of band topology and electronic interactions remains a frontier question. In this work, we predict new interacting electronic orders emerging near higher-order Van Hove singularities present in the Chern bands of the Haldane model. We classify the nature of such singularities and employ unbiased renormalization group methods that unveil a complex landscape of electronic orders, which include ferromagnetism, density-waves and superconductivity. Importantly, we show that repulsive interactions can stabilize long-sought pair-density-wave state and an exotic Chern supermetal, which is a new class of non-Fermi liquid with anomalous quantum Hall response. This framework opens a new path to explore unconventional electronic phases in two-dimensional chiral bands through the interplay of band topology and higher-order Van Hove singularities.

Introduction– The Haldane model [1] provides a minimal description of Chern bands displaying quantized Hall conductance albeit in zero magnetic field, which are realized when Dirac fermions in graphene bands acquire a time-reversal broken, inversion symmetric mass at the two valleys $\pm\boldsymbol{K}$ of the Brillouin zone (BZ). Besides the realization of Haldane Chern bands in ultracold fermions [2], new correlation-driven Chern bands recently identified [3–15] in moiré materials open new paths to explore interaction effects in topological bands. The role of interactions in Haldane Chern bands has received substantial attention. In particular, in the strong coupling regime obtained when the interaction scale U is much stronger than the bandwidth W of a Chern band that is separated from other bands by an energy gap Δ such that $\Delta \gg U \gg W$, electronic correlations can stabilize rich fractionalized phases [16–20]. Furthermore, correlated phases of the repulsive Haldane-Hubbard model at commensurate $1/2$ and $1/4$ fillings have been investigated using numerical methods and mean-field studies [21–29].

On the other hand, defying expectations that the weak coupling regime ($U \ll W$) in Chern bands leads to a stable Fermi liquid (FL) fixed point, recent analysis [30, 31] has uncovered new FL instabilities in partially filled Hofstadter bands [32] (generally supporting non-zero Chern number [33]) due to the interplay of repulsive interactions and logarithmic Van Hove singularities (VHS). In such fractal bands, the magnet flux per unit cell acts a control knob changing the landscape of VHSs and opening new interaction channels. A pressing question then arises: Can VHS catalyze FL instabilities in Haldane Chern bands in the absence of a magnetic field? Notably, while the relation between VHS and electronic correlations has been greatly emphasized in modern 2D materials, from moiré [34–36] to kagomé metals [37, 38], little is known about their influence in Chern bands.

In this Letter, we unveil a new scheme to investigate correlation effects in Chern bands, focusing on the Haldane-Hubbard model as a paradigmatic system to address the confluence of band topology and electronic correlations. Departing from previous studies [21–29], we analyze a new regime characterized by incommensurate fillings reached when the Fermi energy lies near VHS in the Haldane Chern bands. The diverging density of states (DOS) near localized pockets in the BZ allows a treatment of interactions at weak coupling regime using unbiased RG methods. The main results of this work are:

(1) *A novel classification of VHS in Haldane Chern bands:* We analytically identify new logarithmic [39] and higher-order VHS (HOVHS) [40, 41] of Haldane Chern bands, beyond the conventional VHSs in graphene [42]. These new saddle points are controlled by the second neighbor hopping amplitude t_2 and the phase ϕ (see Fig. 1.), which break time reversal symmetry *while preserving spatial inversion.* Notably, we identify a pair of HOVHS at $\pm\boldsymbol{K}$ occurring throughout the boundary of regions II and III of Fig. 1. Such HOVHSs yield diverging DOS $D(\varepsilon) \sim |\varepsilon|^{-1/3}$, promoting strongly enhanced low temperature susceptibilities in all particle-particle and particle-hole channels, which, consequently, open a new path to explore competing electronic orders in Chern bands via these HOVHS.

(2) *Novel FL instabilities through competing orders near HOVHS:* We employ perturbative RG [43, 44] to study FL instabilities in the vicinity of such pair of HOVHS related by inversion symmetry. While this HOVHS 2-patch RG was analyzed in bilayer graphene [40] and moiré systems [45, 46], the situation in Haldane Chern bands is distinct in that *band topology non-trivially constraints the RG flows.* This occurs because the topological winding (± 1) of Haldane Chern bands is associated with electronic wavefunctions on opposite $\pm\boldsymbol{K}$ valleys which have support on opposite sublattices. This entails a form of sublattice interference (SI), which suppresses

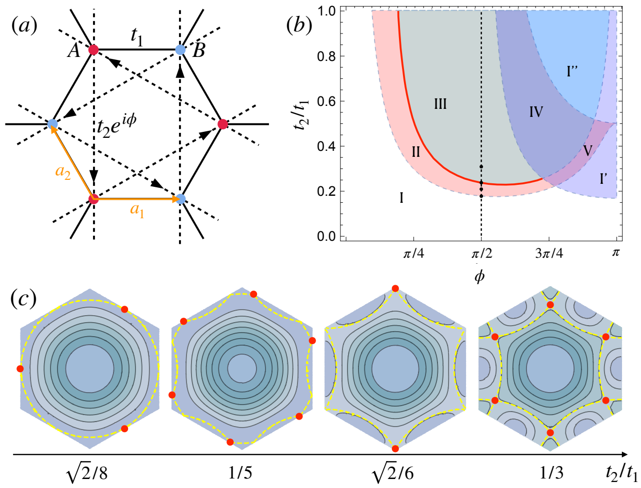

FIG. 1. (a) Lattice model. (b) Landscape of VHSs. The boundary between II and III highlighted in red is where two higher order VHSs located at $\pm\boldsymbol{K}$ emerge. (c) Energy contours show the evolution of VHSs for a fixed $\phi = \pi/2$ but various t, which are marked as the black dots in (b). The yellow dashed curves are the Fermi surfaces at Van Hove filling.

certain interaction channels, profoundly modifying the RG flows and the resulting orders. While this SI was first noticed in the kagome lattice [47–49], to our knowledge, the existence of this important effect and its connection to competing orders in Haldane Chern bands has not received earlier consideration, and is one of the central results of this work.

Incorporating this novel SI into RG analysis brings forth a rich phase diagram, shown in Fig.3, containing a host of ordered phases including ferromagnetism (FM), density-wave (DW), superconductivity (SC) and pair-density-wave (PDW). Remarkably, we also identify a mechanism whereby repulsive interactions can stabilize an exotic interacting supermetal fixed point [50], describing a metallic phase with concomitant divergent susceptibilities but no long-range order, which arises here as a non-Fermi liquid with quantum anomalous Hall response [51]. We coin this new phase a *Chern supermetal*. While the supermetal in [50] relies on an isolated HOVHS (see also [52]), we demonstrate that SI and spontaneous generation of a staggered mass under the RG flow in the Haldane Chern bands is pivotal in suppressing interaction channels between the two HOVHS that would normally drive the system towards an ordered phase [40, 53]. The same mechanism also allows for a pair-density-wave (PDW) state [54] with momentum $\pm\boldsymbol{K}$ to emerge from purely repulsive interactions. Our results thus constitute a new paradigm to explore electronic correlations in topological Chern bands via HOVHS.

Model. We investigate the spin-degenerate single particle Hamiltonian [1]

$$H_0 = \sum_{\sigma=\uparrow,\downarrow}\sum_{\boldsymbol{k}\in\mathrm{BZ}} c^\dagger_{\boldsymbol{k}\sigma}\mathcal{H}_{\boldsymbol{k}}c_{\boldsymbol{k}\sigma}\,, \quad \mathcal{H}_{\boldsymbol{k}} = B_{0,\boldsymbol{k}}\tau_0 + \boldsymbol{B}_{\boldsymbol{k}}\cdot\boldsymbol{\tau}\,, \tag{1}$$

where BZ is the first Brillouin zone, $c_{\boldsymbol{k}\sigma} = (c_{A,\boldsymbol{k},\sigma}, c_{B,\boldsymbol{k},\sigma})^T$ is the fermionic operator on sublattices A and B; τ_μ ($\mu = 0,1,2,3$) represents the 2×2 identity and three Pauli matrices acting on the sublattice degrees of freedom, and

$$B_{0,\boldsymbol{k}} = 2t_2\cos\phi\sum_{i=1}^{3}\cos\boldsymbol{k}\cdot\boldsymbol{b}_i\,,$$

$$\boldsymbol{B}_{\boldsymbol{k}} = \sum_{i=1}^{3}\begin{pmatrix} t_1\cos\boldsymbol{k}\cdot\boldsymbol{a}_i \\ -t_1\sin\boldsymbol{k}\cdot\boldsymbol{a}_i \\ 2t_2\sin\phi\sin\boldsymbol{k}\cdot\boldsymbol{b}_i\end{pmatrix}, \tag{2}$$

where $\boldsymbol{a}_1 = a(1,0)$, $\boldsymbol{a}_2 = \frac{a}{2}(-1,\sqrt{3})$, $\boldsymbol{a}_3 = \frac{a}{2}(-1,-\sqrt{3})$ are vectors connecting A to nearest neighbor B sites and $\boldsymbol{b}_1 = \boldsymbol{a}_2 - \boldsymbol{a}_3, \boldsymbol{b}_2 = \boldsymbol{a}_3 - \boldsymbol{a}_1, \boldsymbol{b}_3 = \boldsymbol{a}_1 - \boldsymbol{a}_2$. a is the lattice constant that we henceforth set to one and we define $t = t_2/t_1$. The single particle Hamiltonian 1 is diagonalized $H_0 = \sum_\sigma\sum_{n=\pm}\varepsilon_{n,\boldsymbol{k}}\psi^\dagger_{n,\sigma,\boldsymbol{k}}\psi_{n,\sigma,\boldsymbol{k}}$ by the unitary transformation $c_{s,\boldsymbol{k},\sigma} = \sum_{n=\pm}u_{sn}(\boldsymbol{k})\psi_{n,\boldsymbol{k},\sigma}$, ($s = A,B$) leading to spin degenerate energy bands $\varepsilon_{\pm,\boldsymbol{k}} = B_{0,\boldsymbol{k}} \pm |\boldsymbol{B}_{\boldsymbol{k}}|$. In order to classify the critical points $\boldsymbol{\nabla}_{\boldsymbol{k}}\varepsilon_{\pm,\boldsymbol{k}} = 0$, we analyse the determinant of the Hessian $\mathbb{H}_{n,\boldsymbol{k}} = \det\left(\frac{\partial^2\varepsilon_{n,\boldsymbol{k}}}{\partial k_i\partial k_j}\right)$, which yields the local minima/maxima ($\mathbb{H}_{n,\boldsymbol{k}} > 0$), conventional saddle points ($\mathbb{H}_{n,\boldsymbol{k}} < 0$) and higher order saddles ($\mathbb{H}_{n,\boldsymbol{k}} = 0$).

Henceforth we focus on the upper band ε_+ with analogous considerations holding for ε_-. The model at $t = 0$ reduces to graphene [42] whose critical points are $\boldsymbol{\Gamma} = (0,0)$, $\pm\boldsymbol{K} = \pm\left(\frac{2\pi}{3},\frac{2\pi}{3\sqrt{3}}\right)$, $\boldsymbol{M}_1 = \left(\frac{2\pi}{3},0\right)$, $\boldsymbol{M}_2 = \left(\frac{\pi}{3},\frac{\pi}{\sqrt{3}}\right)$ and $\boldsymbol{M}_3 = \left(-\frac{\pi}{3},\frac{\pi}{\sqrt{3}}\right)$. $\boldsymbol{\Gamma}$ is the maximum point, the valleys $\pm\boldsymbol{K}$ corresponds to minima and $\boldsymbol{M}_i$ are saddle points. By tracking the behavior of the Hessian at these points, we arrive at the diagram displayed in Fig. 1-(b) (only the region $\phi = [0,\pi]$ is displayed since the Hessian is invariant under $\phi \to 2\pi - \phi$). Analysis of critical points reveals:

Regions I, I′ and I″: In these, $\boldsymbol{M}_i$ are saddle points. In I, Γ is a maximum and $\pm\boldsymbol{K}$ are minima; this pattern reverses in I′ and I″. The boundary between regions I and II is defined by $t = \tau_{12}(\phi) = \frac{1}{32\sin^2\phi}\left[\cos\phi + \sqrt{\cos^2\phi + 32\sin^2\phi}\right]$, along which the Hessian vanishes, signaling a HOVHS as shown in the first panel of Fig. 1-(c) In particular, at $\phi = \pi/2$, $\varepsilon_+(\boldsymbol{M}_1+\boldsymbol{p}) \approx \varepsilon_+(\boldsymbol{M}_1) + (9/4)p_x^2 - (27/16)p_x^2p_y^2$ describes a HOVHS with $D(\varepsilon) \sim |\varepsilon|^{-1/4}$.

Region II: Crossing the boundary into region II, where $t > \tau_{12}(\phi)$, each HOVHS splits into two conventional VHS equidistant from $\boldsymbol{M}_i$ on the BZ boundary. As we increase t and get closer to the boundary with region

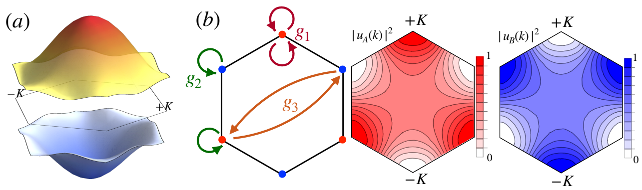

FIG. 2. (a) Band structure with HOVHS at $\phi = \pi/2$. (b) Two patch model of the HOVHS and the sublattice weight for the upper band.

III, the VHS tend towards the $\pm\boldsymbol{K}$ (second panel of Fig. 1-(c)).

Region III: The boundary between II and III is defined by $t = \tau_{23}(\phi) = 3^{1/4}[18\sqrt{3}\sin^2\phi - 18|\sin\phi|\cos\phi]^{-1/2}$ where the Hessian vanishes when evaluated at the BZ zone corners $\pm\boldsymbol{K}$. We note that this curve has an asymptote at $\phi = \pi/6$. Along the curve $\tau_{23}(\phi)$, $\pm\boldsymbol{K}$ are HOVHSs with $D(\varepsilon) \sim |\varepsilon|^{-1/3}$ (third panel of Fig.1-(c)), which separate region II and III where $\pm\boldsymbol{K}$ are local minima or maxima, respectively. As we cross the boundary into region (III), the VHSs split from the $\pm\boldsymbol{K}$ points and move towards the center of the BZ (last panel in Fig. 1-(c)). We note that regions IV and V are similar to III and II, except for the existence of 2 groups of six quasidegenerate VHS, but they are not the focus of this work.

Two HOVHS patches: Henceforth, we focus on the boundary between II and III, where a pair of HOVHS are located at $\pm\boldsymbol{K}$ for each band. A typical band structure for $\phi = \pi/2$ is presented in Fig.2(a). Without loss of generality, we focus on the upper band (orange band in the figure). Close to HOVHS filling, we can effectively expand the dispersion within small patches centered at $\pm\boldsymbol{K}$ up to fourth order:

$$\varepsilon_{\pm\boldsymbol{K}}(\boldsymbol{p}) = \varepsilon_0 \pm \kappa_1(p_y^3 - 3p_x^2 p_y) - \kappa_2(p_x^2 + p_y^2)^2\,, \tag{3}$$

where ε_0 is the energy at the HOVHS, $\kappa_1 = \frac{9t\cos\phi}{8} + \frac{\sqrt{3}|\sin\phi|(6t^2+\csc^2\phi)}{16t}$ and $\kappa_2 = \frac{27}{64}t\cos\phi - \frac{|\sin\phi|(162t^4+27t^2\csc^2\phi-\csc^4\phi)}{128\sqrt{3}t^3}$ are two coefficients that vary continuously along the boundary between II and III, determined by the curve $t = \tau_{23}(\phi)$. $\kappa_2 \neq 0$ quantifies the deviation from perfect nesting, which occurs at $(\phi, t) = (\pi/6, \tau_{23}(\pi/6))$.

This two patch model admits three momentum conserving interactions g_1, g_2 and g_3 (see Fig.2(b)) defined as

$$H_I = g_1\psi_\alpha^\dagger\psi_\alpha^\dagger\psi_\alpha\psi_\alpha + \sum_{\alpha\neq\beta} g_2\psi_\alpha^\dagger\psi_\beta^\dagger\psi_\beta\psi_\alpha + g_3\psi_\alpha^\dagger\psi_\beta^\dagger\psi_\alpha\psi_\beta \tag{4}$$

where we leave the spin structure and spin summation implicit, which should be $\sigma, \sigma', \sigma', \sigma$ for the four fermions operators in each term, and denote the patches by $\alpha, \beta = \pm$ with $\psi_\pm = \psi_{\pm\boldsymbol{K}+\boldsymbol{p}}$. These interactions are obtained from projecting the lattice fermion interactions onto band fermions. Quite interestingly, as long as we focus on patches around $\pm\boldsymbol{K}$, the *SI effect always associates each valley with a distinct sublattice index.* We show this effect by plotting the sublattice weights (for the upper band) $|u_{A+}(\boldsymbol{k})|^2$ (red) and $|u_{B+}(\boldsymbol{k})|^2$ (blue) in Fig.2(b). Crucially, fermions near $+\boldsymbol{K}$ ($-\boldsymbol{K}$) are solely from A (B) sublattice, so there is a one-to-one correspondence between $c_{i\in A/B}$ and ψ_α. An important consequence is that the onsite Hubbard interaction $H_U = U\sum_i c_{i\uparrow}^\dagger c_{i\downarrow}^\dagger c_{i\downarrow}c_{i\uparrow}$ only contributes to g_1 and the nearest neighbor interaction $H_V = V\sum_{\langle ij\rangle} c_{i\sigma}^\dagger c_{j\sigma'}^\dagger c_{j\sigma'}c_{i\sigma}$ only contributes to g_2. Note that if there were no SI, H_U would contribute to all g_i. Moreover, the SI also implies that g_3 only arises from the more exotic bond-bond interactions $H_W = W\sum_{\langle ij\rangle} c_{i\sigma}^\dagger c_{j\sigma'}^\dagger c_{i\sigma'}c_{j\sigma}$ [55–57]. In the extended-Hubbard model with additional bond-bond interactions ($H_U + H_V + H_W$) the bare interactions before renormalization are therefore

$$g_1(0) = U,\;\; g_2(0) = V,\;\; g_3(0) = W. \tag{5}$$

Note that this initial condition is robust against imperfect nesting, as long as the two HOVHS are located at $\pm\boldsymbol{K}$. The bond-bond interactions are typically orders of magnitude smaller than other interactions [58, 59], and so we will neglect them below.

RG equations: To identify the potential electronic instabilities resulting from these interactions in Eq.(5), we note that in the presence of HOVHS the bare particle-hole and particle-particle bubbles at zero momentum or $\pm\boldsymbol{K}$ all diverge in the same power-law manner. These bubbles constitute the renormalization of g_i's at one-loop level, resulting in the following RG flow equations [40, 46]:

$$\begin{aligned}\dot{g_1} &= \epsilon g_1 + (d_2 - d_3)g_1^2 - 2d_2 g_2^2\,,\\ \dot{g_2} &= \epsilon g_2 + (d_1 - 1)g_2^2 - 2d_2 g_1 g_2.\end{aligned} \tag{6}$$

Here we defined the running parameter as $y = \Pi_{pp}(\boldsymbol{q} = 0)$, and the nesting parameters are defined as $d_1 \approx \Pi_{ph}(\boldsymbol{K})/y$, $d_2 \approx \Pi_{ph}(0)/y$ and $d_3 \approx \Pi_{pp}(\boldsymbol{K})/y$. Within our patch model, these bubbles are calculated via

$$\begin{aligned}&\Pi_{pp}(0)\,, \Pi_{pp}(\boldsymbol{K}) = \int_{\boldsymbol{p}} \frac{1 - f[\epsilon_{\boldsymbol{K}}(\boldsymbol{p})] - f[\epsilon_{\mp\boldsymbol{K}}(-\boldsymbol{p})]}{\epsilon_{\boldsymbol{K}}(\boldsymbol{p}) + \epsilon_{\mp\boldsymbol{K}}(-\boldsymbol{p})},\\ &\Pi_{ph}(\boldsymbol{K}) = \int_{\boldsymbol{p}} \frac{f[\epsilon_{-\boldsymbol{K}}(\boldsymbol{p})] - f[\epsilon_{\boldsymbol{K}}(\boldsymbol{p})]}{\epsilon_{\boldsymbol{K}}(\boldsymbol{p}) - \epsilon_{-\boldsymbol{K}}(\boldsymbol{p})},\; \Pi_{ph}(0) = \int_{\boldsymbol{p}} \frac{-\partial f[\epsilon]}{\partial\epsilon}\end{aligned} \tag{7}$$

where $\int_{\boldsymbol{p}} = \int_{|\boldsymbol{p}|<\Lambda} \frac{d^2\boldsymbol{p}}{4\pi^2}$ with Λ being the high energy cutoff, and in the first line '+' is for $\Pi_{pp}(\boldsymbol{K})$ while '-' is for $\Pi_{pp}(0)$. In the perfect nesting case when κ_2 in Eq.(3) vanishes, Eq.(7) can be evaluated analytically, which leads to $d_1 = 1$, $d_2 = d_3 \approx \frac{1}{3}$. But in general d_i's are determined by both the energy scale and the parameter ϕ and can strongly deviate from their perfect nesting values. The tree-level term ϵ results from rescaling the field operators, with $\epsilon = 0$ for the Gaussian fixed point and $\epsilon = 1/3$ for the supermetal fixed point, which occurs at $g_2 = 0$, $g_1 = \frac{1}{3(d_3-d_2)}$. Note that the strong coupling fixed points are the same for both choices.

To probe possible symmetry breaking orders, we introduce the following order parameters in both particle-particle and particle-hole channels:

$$
\begin{aligned}
&\Delta^{s}_{\text{SC}} = \langle \psi^\dagger_+ \psi^\dagger_- + \psi^\dagger_- \psi^\dagger_+ \rangle, \;\; \Delta^{t}_{\text{SC}} = \langle \psi^\dagger_+ \psi^\dagger_- - \psi^\dagger_- \psi^\dagger_+ \rangle \\
&\Delta_{\text{PDW}} = \langle \psi_\alpha \psi_\alpha \rangle, \;\; \Delta_{\text{CDW}} = \langle \psi^\dagger_+ \psi_- \rangle, \;\; \Delta_{\text{SDW}} = \langle \psi^\dagger_+ \hat{s} \psi_- \rangle \\
&\Delta_{\text{FM1}} = \sum_\alpha \langle \psi^\dagger_\alpha s_z \psi_\alpha \rangle, \;\; \Delta_{\text{FM2}} = \sum_\alpha \alpha \langle \psi^\dagger_\alpha s_z \psi_\alpha \rangle \\
&\Delta_{\text{PI1}} = \langle \psi^\dagger_+ \psi_+ + \psi^\dagger_- \psi_- \rangle, \;\; \Delta_{\text{PI2}} = \langle \psi^\dagger_+ \psi_+ - \psi^\dagger_- \psi_- \rangle .
\end{aligned} \tag{8}
$$

These are singlet and triplet uniform superconductivity $\Delta^{s/t}_{\text{SC}}$, finite momentum superconductivity (pair density wave) Δ_{PDW}, charge- and spin-density wave $\Delta_{\text{C/SDW}}$, ferromagnetism with different parities $\Delta_{\text{FM1/2}}$ and Pomeranchuk instabilities with different parities $\Delta_{\text{PI1/2}}$. Note that Δ_{PI1} amounts to shift the chemical potential by an overall constant, while Δ_{PI2} corresponds to shifting the chemical potentials at $\pm\boldsymbol{K}$ oppositely. In other words, in the presence of $\Delta_{\text{PI1/2}}$, the system can still remain metallic but is shifted away from the Van Hove filling. When the energy scale is reduced, the order parameters flow as

$$
\begin{aligned}
&\dot{\Delta}^{s/t}_{\text{SC}} = -g_2 \Delta^{s/t}_{\text{SC}}, \;\; \dot{\Delta}_{\text{PDW}} = -d_3 g_1 \Delta_{\text{PDW}}, \\
&\dot{\Delta}_{\text{C/SDW}} = d_1 g_2 \Delta_{\text{C/SDW}}, \;\; \dot{\Delta}_{\text{FM1/2}} = d_2 g_1 \Delta_{\text{FM1/2}}, \\
&\dot{\Delta}_{\text{PI1}} = d_2(-g_1 - 2g_2)\Delta_{\text{PI1}}, \;\; \dot{\Delta}_{\text{PI2}} = d_2(-g_1 + 2g_2)\Delta_{\text{PI2}}.
\end{aligned} \tag{9}
$$

Lastly, we will use the renormalized susceptibilities to identify the leading order, which obey $\dot{\chi}_i = d_i |\Delta_i|^2$, where d_i is the corresponding nesting parameters while for the uniform SC we have $d_i = 1$. Close to the onset of the instability, $\chi_i \sim (y_c - y)^{\gamma_i}$, thus the most negative γ_i corresponds to the leading instability.

Phase diagram and two-step RG: In Fig.3 (a) we present the phase diagram for the bare couplings $g_j(0)$ with tree level contribution for $\phi = \pi/2$ and $T = 0.001t$. The RG flows are also shown by the stream lines. There are three regions in the phase diagram: two regions with strong coupling instabilities (blue for $g_2 > 0$ and red for $g_2 < 0$) in which orders develop, and a region (green) within which no instability of the HOVHS develops and no symmetry is broken, resulting in a supermetal phase. Note that the slopes of the boundaries between the regions are functions of ϕ and T, but all phase diagrams are qualitatively similar. In particular, the boundaries are given by $g_2 = \left(1 - d_1 \pm \sqrt{(1-d_1)^2 + 8(3d_2 - d_3)}\right) g_1/(4d_2)$ for $g_1 > 0$.

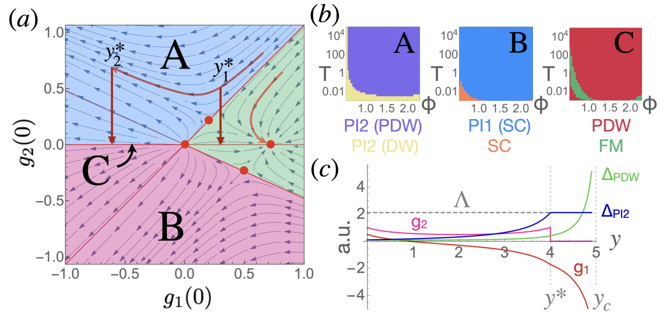

FIG. 3. (a) $g_1(0) = U$, $g_2(0) = V$ phase diagram and RG flow trajectories. Fixed points are shown by red dots, fixed trajectories are shown by red lines that also form the phase boundaries. All trajectories in the green region flow to the supermetal fixed point, while all trajectories in the blue region A with $g_2 > 0$ (red region B with $g_2 < 0$) flow to some symmetry-broken strong coupling fixed point. The corresponding phases depend on temperature T and ϕ, as shown in (b): the PI2 instability is always leading in A with a subleading PDW (purple) or C/SDW (yellow, labeled DW) instability; either a leading PI1 with subleading s/tSC or a leading s/tSC occur in B. The fixed trajectory along $g_2 = 0$ is unstable but can become stabilized at $y = y^*$ due to a staggered mass generated by the PI2 instability becoming comparable to the RG cutoff Λ, as shown in (c), which also shows the RG flows of g_1 and g_2 starting in region A with repulsive bare interactions. Depending on whether g_1 changes sign or not at y^* (y_2^* and y_1^* labeled in (a)), either an instability in region C (PDW or FM) or a supermetal phase is realized respectively.

The symmetry broken phases within each region for different values of ϕ and temperature are shown in Fig.3(b). For $g_2 < 0$ (region B), singlet and triplet superconductivities are the leading symmetry-breaking instabilities (PI1, corresponding to a chemical potential, is generally the leading vertex correction but does not break any symmetry and does not gap out the Fermi surface). The degeneracy is lifted by the neglected bond-bond interaction giving a non-zero $W = g_3$, with positive (negative) values favoring triplet (singlet) SC. For $g_2 > 0$ (region A), the leading instability is the inversion-symmetry breaking valley-order PI2, with subleading PDW or C/SDW as shown in Fig.3 (b); observe that C/SDW are Kekulé-type bond orders due to the sublattice-valley polarization. These are consistent with the phases found in [46].

We note, however, that the PI2 instability does not gap out the HOVHS, but yields an interaction-driven staggered mass in the Haldane model. Once the generated staggered mass M is sufficiently large, the RG equations Eq. 6 are no longer valid, as only a single HOVHS at a single valley can be tuned to at a time, resulting in the situation considered in [52]. In that case the g_2 and g_3 processes become forbidden by momentum conservation. This results in a particularly interesting scenario for the most relevant case of completely repulsive interactions (positive g_j). The instabilities in RG generally occur at some finite critical value $y = y_c$, but it is possible that at some point the running $M(y)$ grows larger than the cutoff $\Lambda = \Lambda_0 e^{-y}$ (Λ_0 being the bare cut-off prior to starting the RG flow) for some $y^* < y_c$, in which case the RG should be done in two steps as illustrated in Fig.3(c). When y^* is reached, Eq. 6 has to be modified with $g_2 \to 0$, with the new RG flow continuing along the $g_2 = 0$ line in the phase diagram (region C), which is otherwise an unstable fixed trajectory of the RG flow, until y_c is finally reached.

Depending on whether $g_1(y^*)$ is positive or negative, this mechanism can realize a Chern supermetal or a broken symmetry phase, respectively. The possible symmetry broken phases are shown in the third panel of Fig.3(b), and include either a FM or PDW instabilities. We emphasize that these phases would be unstable in the absence of the interaction-generated staggered mass which projects out the g_2 and the previously neglected g_3 interactions. For the supermetal, g_3 in principle leads to a further instability [40, 46] due to multiple HOVHS [53]. As the bond-bond interactions $W = g_3(0)$ are presumed very small, however, the resulting instability may only occur at exceedingly low temperatures making the supermetal stable at finite temperature even in the absence of a generated staggered mass, thanks to the SI mechanism. The PDW phase is similarly stabilized once g_2 and g_3 are projected out, but importantly g_1 changes sign before the projection, with attraction in the PDW channel thus generated by purely repulsive bare interactions. This scenario contrasts with models with a single HOVHS [46, 52], where the PDW instability requires bare attractive interactions.

In summary, we have classified the manifold of VHSs in inversion symmetric Haldane bands, uncovering a symbiotic relation between topology and SI due to the presence of HOVHS at the high-symmetry points supporting Dirac fermions in the absence of the topological mass, which provides a route to study the interplay of interactions and band topology once the Fermi energy lies in the vicinity of these higher-order saddles. Beyond a host of exotic ordered phases including long-sought pair-density waves, we identified a novel Chern supermetal displaying non-Fermi liquid behavior and quantum anomalous Hall response, which are salient features observable in transport and tunneling experiments. Generalizing this framework to other band structures where the HOVHS lie at high-symmetry points [60] will be a promising route to explore interacting phases in other topological bands realized either in ultracold fermions or in 2D Van der Waals materials.

ACKNOWLEDGMENTS

We thank Claudio Chamon, Dmitry Chichinadze and Ajit Srivastava for useful discussions. This research was supported by the U.S. Department of Energy, Office of Science, Basic Energy Sciences, under Award DE-SC0023327 (D.S. and L.H.S.) and by the Gordon and Betty Moore FoundationâĂŹs EPiQS Initiative through GBMF8686 (Y.-M.W).

[1] F. D. M. Haldane, Phys. Rev. Lett. **61**, 2015 (1988).

[2] G. Jotzu, M. Messer, R. Desbuquois, M. Lebrat, T. Uehlinger, D. Greif, and T. Esslinger, Nature **515**, 237 (2014).

[3] E. M. Spanton, A. A. Zibrov, H. Zhou, T. Taniguchi, K. Watanabe, M. P. Zaletel, and A. F. Young, Science **360**, 62 (2018), https://science.sciencemag.org/content/360/6384/62.full.pdf.

[4] A. L. Sharpe, E. J. Fox, A. W. Barnard, J. Finney, K. Watanabe, T. Taniguchi, M. A. Kastner, and D. Goldhaber-Gordon, Science **365**, 605 (2019), publisher: American Association for the Advancement of Science.

[5] M. Serlin, C. L. Tschirhart, H. Polshyn, Y. Zhang, J. Zhu, K. Watanabe, T. Taniguchi, L. Balents, and A. F. Young, Science **367**, 900 (2020), publisher: American Association for the Advancement of Science.

[6] Y. Saito, J. Ge, L. Rademaker, K. Watanabe, T. Taniguchi, D. A. Abanin, and A. F. Young, Nature Physics **17**, 478 (2021).

[7] Y. Xie, A. T. Pierce, J. M. Park, D. E. Parker, E. Khalaf, P. Ledwith, Y. Cao, S. H. Lee, S. Chen, P. R. Forrester, K. Watanabe, T. Taniguchi, A. Vishwanath, P. Jarillo-Herrero, and A. Yacoby, Nature **600**, 439 (2021).

[8] K. P. Nuckolls, M. Oh, D. Wong, B. Lian, K. Watanabe, T. Taniguchi, B. A. Bernevig, and A. Yazdani, Nature **588**, 610 (2020), number: 7839 Publisher: Nature Publishing Group.

[9] S. Wu, Z. Zhang, K. Watanabe, T. Taniguchi, and E. Y. Andrei, Nature Materials , 1 (2021), publisher: Nature Publishing Group.

[10] I. Das, X. Lu, J. Herzog-Arbeitman, Z.-D. Song, K. Watanabe, T. Taniguchi, B. A. Bernevig, and D. K. Efetov, Nature Physics **17**, 710 (2021), number: 6 Publisher: Nature Publishing Group.

[11] Y. Choi, H. Kim, Y. Peng, A. Thomson, C. Lewandowski, R. Polski, Y. Zhang, H. S. Arora, K. Watanabe, T. Taniguchi, J. Alicea, and S. Nadj-Perge, Nature **589**, 536 (2021).

[12] J. M. Park, Y. Cao, K. Watanabe, T. Taniguchi, and P. Jarillo-Herrero, Nature **592**, 43 (2021), number: 7852 Publisher: Nature Publishing Group.

[13] P. Stepanov, M. Xie, T. Taniguchi, K. Watanabe, X. Lu, A. H. MacDonald, B. A. Bernevig, and D. K. Efetov, Phys. Rev. Lett. **127**, 197701 (2021).

[14] A. T. Pierce, Y. Xie, J. M. Park, E. Khalaf, S. H. Lee, Y. Cao, D. E. Parker, P. R. Forrester, S. Chen, K. Watanabe, T. Taniguchi, A. Vishwanath, P. Jarillo-Herrero, and A. Yacoby, Nature Physics **17**, 1210 (2021), number: 11 Publisher: Nature Publishing Group.

[15] J. Yu, B. A. Foutty, Z. Han, M. E. Barber, Y. Schattner, K. Watanabe, T. Taniguchi, P. Phillips, Z.-X. Shen, S. A. Kivelson, and B. E. Feldman, (2021), 10.48550/ARXIV.2108.00009.
[16] T. Neupert, L. Santos, C. Chamon, and C. Mudry, Phys. Rev. Lett. **106**, 236804 (2011).
[17] D. N. Sheng, Z.-C. Gu, K. Sun, and L. Sheng, Nature Communications **2**, 389 EP (2011).
[18] E. Tang, J.-W. Mei, and X.-G. Wen, Phys. Rev. Lett. **106**, 236802 (2011).
[19] K. Sun, Z. Gu, H. Katsura, and S. Das Sarma, Phys. Rev. Lett. **106**, 236803 (2011).
[20] Y.-F. Wang, Z.-C. Gu, C.-D. Gong, and D. Sheng, Physical review letters **107**, 146803 (2011).
[21] P. Mai, B. E. Feldman, and P. W. Phillips, Phys. Rev. Res. **5**, 013162 (2023).
[22] J. He, S.-P. Kou, Y. Liang, and S. Feng, Phys. Rev. B **83**, 205116 (2011).
[23] W. Zheng, H. Shen, Z. Wang, and H. Zhai, Phys. Rev. B **91**, 161107 (2015).
[24] J. Wu, J. P. L. Faye, D. Sénéchal, and J. Maciejko, Physical Review B **93**, 075131 (2016).
[25] V. S. Arun, R. Sohal, C. Hickey, and A. Paramekanti, Phys. Rev. B **93**, 115110 (2016).
[26] T. I. Vanhala, T. Siro, L. Liang, M. Troyer, A. Harju, and P. Törmä, Phys. Rev. Lett. **116**, 225305 (2016).
[27] J. Imriška, L. Wang, and M. Troyer, Phys. Rev. B **94**, 035109 (2016).
[28] I. S. Tupitsyn and N. V. Prokof'ev, Physical Review B **99**, 121113 (2019).
[29] T.-C. Yi, S. Hu, E. V. Castro, and R. Mondaini, Phys. Rev. B **104**, 195117 (2021).
[30] D. Shaffer, J. Wang, and L. H. Santos, Nature Communications **13**, 7785 (2022).
[31] D. Shaffer and L. H. Santos, arXiv preprint arXiv:2210.16324 (2022).
[32] D. R. Hofstadter, Physical Review B **14**, 2239 (1976), publisher: American Physical Society.
[33] D. J. Thouless, M. Kohmoto, M. P. Nightingale, and M. den Nijs, Physical Review Letters **49**, 405 (1982), publisher: American Physical Society.
[34] G. Li, A. Luican, J. Lopes dos Santos, A. Castro Neto, A. Reina, J. Kong, and E. Andrei, Nature physics **6**, 109 (2010).
[35] A. Kerelsky, L. J. McGilly, D. M. Kennes, L. Xian, M. Yankowitz, S. Chen, K. Watanabe, T. Taniguchi, J. Hone, C. Dean, A. Rubio, and A. N. Pasupathy, Nature **572**, 95 (2019).
[36] S. Wu, Z. Zhang, K. Watanabe, T. Taniguchi, and E. Y. Andrei, Nature materials **20**, 488 (2021).
[37] M. Kang, S. Fang, J.-K. Kim, B. R. Ortiz, S. H. Ryu, J. Kim, J. Yoo, G. Sangiovanni, D. Di Sante, B.-G. Park, *et al.*, Nature Physics **18**, 301 (2022).
[38] T. Neupert, M. M. Denner, J.-X. Yin, R. Thomale, and M. Z. Hasan, Nature Physics **18**, 137 (2022).
[39] L. Van Hove, Phys. Rev. **89**, 1189 (1953).
[40] A. Shtyk, G. Goldstein, and C. Chamon, Physical Review B **95**, 035137 (2017).
[41] N. F. Yuan, H. Isobe, and L. Fu, Nature communications **10**, 5769 (2019).
[42] A. C. Neto, F. Guinea, N. M. Peres, K. S. Novoselov, and A. K. Geim, Reviews of modern physics **81**, 109 (2009).
[43] R. Shankar, Reviews of Modern Physics **66**, 129 (1994).
[44] S. Maiti and A. V. Chubukov, AIP Conference Proceedings **1550**, 3 (2013), publisher: American Institute of Physics.
[45] Y.-T. Hsu, F. Wu, and S. Das Sarma, Phys. Rev. B **104**, 195134 (2021).
[46] Z. Wu, Y.-M. Wu, and F. Wu, Phys. Rev. B **107**, 045122 (2023).
[47] M. L. Kiesel and R. Thomale, Physical Review B **86**, 121105 (2012).
[48] Y.-M. Wu, R. Thomale, and S. Raghu, arXiv preprint arXiv:2211.01388 (2022).
[49] T. Schwemmer, H. Hohmann, M. DÃijrrnagel, J. Potten, J. Beyer, S. Rachel, Y.-M. Wu, S. Raghu, T. MÃijller, W. Hanke, and R. Thomale, "Pair density wave instability in the kagome hubbard model," (2023), arXiv:2302.08517 [cond-mat.str-el].
[50] H. Isobe and L. Fu, Phys. Rev. Res. **1**, 033206 (2019).
[51] N. Nagaosa, J. Sinova, S. Onoda, A. H. MacDonald, and N. P. Ong, Rev. Mod. Phys. **82**, 1539 (2010).
[52] Ã. M. Aksoy, A. Chandrasekaran, A. Tiwari, T. Neupert, C. Chamon, and C. Mudry, (2023), 10.48550/ARXIV.2302.04877.
[53] L. Classen, A. V. Chubukov, C. Honerkamp, and M. M. Scherer, Physical Review B **102**, 125141 (2020), publisher: American Physical Society.
[54] D. F. Agterberg, J. S. Davis, S. D. Edkins, E. Fradkin, D. J. Van Harlingen, S. A. Kivelson, P. A. Lee, L. Radzihovsky, J. M. Tranquada, and Y. Wang, Annual Review of Condensed Matter Physics **11**, 231 (2020).
[55] S. Kivelson, W.-P. Su, J. R. Schrieffer, and A. J. Heeger, Phys. Rev. Lett. **58**, 1899 (1987).
[56] S. Kivelson, W. P. Su, J. R. Schrieffer, and A. J. Heeger, Phys. Rev. Lett. **60**, 72 (1988).
[57] M. Nakamura and K. Itoh, Journal of the Physical Society of Japan **70**, 3606 (2001), https://doi.org/10.1143/JPSJ.70.3606.
[58] J. Hubbard and B. H. Flowers, Proceedings of the Royal Society of London. Series A. Mathematical and Physical Sciences **276**, 238 (1963), https://royalsocietypublishing.org/doi/pdf/10.1098/rspa.1963.0204.
[59] J. T. Gammel and D. K. Campbell, Phys. Rev. Lett. **60**, 71 (1988).
[60] A. Chandrasekaran, A. Shtyk, J. J. Betouras, and C. Chamon, Physical Review Research **2**, 013355 (2020).